

Anomalous localization in a kicked quasicrystal

Received: 2 May 2022

Accepted: 8 November 2023

Published online: 17 January 2024

 Check for updates

Toshihiko Shimasaki¹, Max Prichard^{1,4}, H. Esat Kondakci^{1,4}, Jared E. Pagett^{1,4}, Yifei Bai^{1,4}, Peter Dotti¹, Alec Cao¹, Anna R. Dardia¹, Tsung-Cheng Lu², Tarun Grover³ & David M. Weld¹✉

Quantum transport can distinguish between dynamical phases of matter. For instance, ballistic propagation characterizes the absence of disorder, whereas in many-body localized phases, particles do not propagate for exponentially long times. Additional possibilities include states of matter exhibiting anomalous transport in which particles propagate with a non-trivial exponent. Here we report the experimental observation of anomalous transport across a broad range of the phase diagram of a kicked quasicrystal. The Hamiltonian of our system has been predicted to exhibit a rich phase diagram, including not only fully localized and fully delocalized phases but also an extended region comprising a nested pattern of localized, delocalized and multifractal states, which gives rise to anomalous transport. Our cold-atom realization is enabled by new Floquet engineering techniques, which expand the accessible phase diagram by five orders of magnitude. Mapping transport properties throughout the phase diagram, we observe disorder-driven re-entrant delocalization and sub-ballistic transport, and we present a theoretical explanation of these phenomena based on eigenstate multifractality.

Although transport-based diagnostics of static quantum phases^{1–4} generally reveal anomalous transport regimes only if the system is fine-tuned to a critical point^{5–8}, externally driven quantum matter⁹ can exhibit exotic states with no equilibrium counterpart. As we demonstrate in this work, driven systems can thus open up the exploration of new states of matter characterized by an intricate interplay of fractal structure and quantum dynamics.

The time-independent Aubry–André–Harper (AAH) Hamiltonian^{10,11} describes particles hopping in a one-dimensional lattice with quasiperiodic pseudo-disorder. This paradigmatic model of quantum transport and quantum Hall phenomena exhibits Hofstadter butterfly energy spectra and hosts multifractal eigenstates only at a duality-protected localization phase transition^{10–13}. If the incommensurate potential is applied instead as brief periodic kicks, the resulting ‘occasional quasicrystal’ described by the kicked Aubry–André–Harper

(kAAH) model epitomizes the interplay between disorder and driving in quantum matter. Although pioneering experiments in various platforms have explored static and sinusoidally driven AAH models and incommensurate kicked rotors^{14–20}, the kAAH model has previously been explored only theoretically^{21–28}.

We demonstrate experimentally that the kAAH model exhibits signatures of anomalous transport across an extended range of parameter space, in agreement both with numerical calculations and with theoretical expectations for related models^{21–24}. This letter reports three interconnected advances. The first is the experimental realization of the kAAH model itself. The second is the development of apodized Floquet engineering techniques that use spectrally tailored pulses to extend the accessible parameter range of our quantum simulator into the region where an extended regime of anomalous transport is theoretically expected. The third main advance is the measurement of

¹Department of Physics, University of California, Santa Barbara, CA, USA. ²Perimeter Institute for Theoretical Physics, Waterloo, Ontario, Canada.

³Department of Physics, University of California at San Diego, La Jolla, CA, USA. ⁴These authors contributed equally: Max Prichard, H. Esat Kondakci, Jared E. Pagett, Yifei Bai. ✉e-mail: weld@ucsb.edu

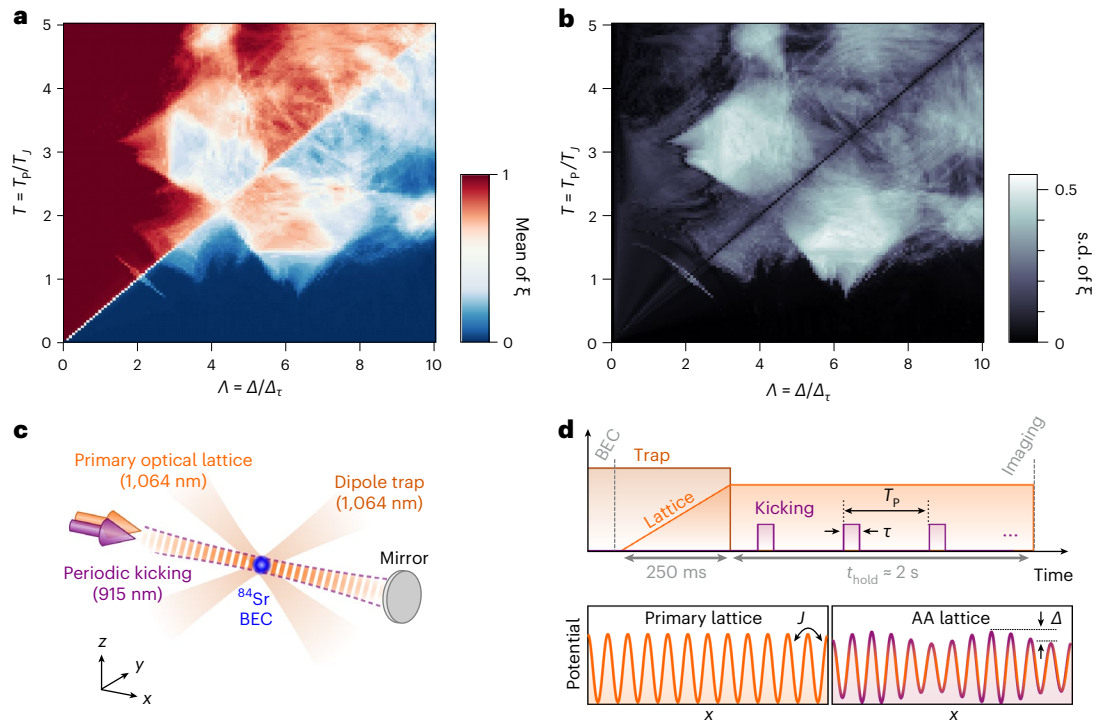


Fig. 1 | Phase diagram of the kAAH model and experimental approach. a, Average IPR scaling exponent ξ as a function of Λ and T , for $\alpha = 1.162842$. **b**, Standard deviation of IPR scaling exponents. Along the diagonal ($\Lambda/T = 2$), the scaling exponents for all eigenvectors take a single value. **c**, Schematic of the experiment. **d**, Experimental sequence. AA, Aubry–André.

the global phase diagram of the kAAH model, which reveals re-entrant delocalization and an extended parameter regime of anomalous transport that we argue theoretically is a consequence of multifractal states.

The experiments begin by loading a Bose–Einstein condensate (BEC) of a tunable number of ^{84}Sr atoms (typically around 2×10^5) into the ground band of a $10E_r$ -deep primary optical lattice, where $E_r = \hbar^2/2m\lambda_p^2$ is the recoil energy, m is the atomic mass, \hbar is Planck’s constant and $\lambda_p = 1,063.9774(23)$ nm is the primary lattice laser wavelength. To implement the kAAH Hamiltonian, pulsed incommensurate pseudo-disorder is realized by periodically applying a separate overlapped optical lattice of wavelength $\lambda_s = 914.4488(17)$ nm. The kAAH Hamiltonian thus realized is given in the tight-binding approximation by

$$\hat{H} = -J \sum_{i=1}^L (\hat{b}_i^\dagger \hat{b}_{i+1} + \text{h.c.}) + F(t)\Delta \sum_{i=1}^L \cos(2\pi\alpha i + \varphi) \hat{b}_i^\dagger \hat{b}_i, \quad (1)$$

where $J = 0.0192E_r \approx \hbar \times 40$ Hz is the tunnelling energy, which gives rise to a tunnelling time $T_J = \hbar/J = (1/2\pi) \times 25$ ms, \hat{b}_i (\hat{b}_i^\dagger) is the bosonic annihilation (creation) operator at the i -th lattice site, Δ is the disorder strength, $\alpha = \lambda_p/\lambda_s$ is the wavelength ratio of the two lattices, φ is the relative phase of the two lattices, and $F(t) = \sum_n f_\tau(t - nT_p)$ is the waveform of a periodic pulse train composed of finite-width, unit-height pulses with an effective pulse width $\tau = \int f_\tau(t) dt$ and pulse interval T_p (Supplementary Information section II). As we will discuss, proper selection of the form of $f_\tau(t)$ is crucial for exploring the majority of the phase diagram. We study the phase diagram in a two-dimensional parameter space with dimensionless axes $T = T_p/T_J = T_p/\hbar$ and $\Lambda = \Delta/\Delta_\tau = \Delta\tau/\hbar$, which characterize the kick period and kick strength, respectively. To map out this phase diagram, we measure the long-time evolution of the density distribution of an initial tightly confined wave packet for different T and Λ using in situ absorption imaging^{14,29,30}.

Theory predicts a rich phase diagram for this experimentally unexplored model^{26,27}. In the high-frequency limit ($1/T \gg 1$), the model

reduces to the static AAH Hamiltonian. Much richer behaviours emerge at larger values of T and Λ (Fig. 1a,b). Numerically analysing the inverse participation ratio (IPR) $\sum_{j=1}^L |\psi_j|^4 \approx L^{-\xi}$ of single-particle position-space eigenstates ψ_j , we find four regimes in the (Λ, T) plane, in agreement with previous analyses of the equivalent quantum chaotic kicked Harper model^{21–25,31}. The regime with $T \gg \Lambda$ is a completely delocalized phase in which the IPR exponent averaged over all states $\xi = 1$. This and a duality mapping (Supplementary Information section I B) implies a localized phase ($\xi = 0$) for $T \ll \Lambda$. Between these two limits, for sufficiently large T and Λ , there is an extended parameter range in which localized and delocalized states coexist in an intricate nested pattern with a finite fraction of multifractal states (Extended Data Fig. 1)^{25,31}. At constant T (for example, $T = 1.5$), the predicted average IPR exponents and fraction of localized states can depend non-monotonically on Λ , suggesting the possibility of anomalous ‘re-entrant’³² states in which continuously increasing disorder strength can drive localization, then delocalization and then re-localization. In the thermodynamic limit, multifractality is theoretically expected to persist along the self-dual line $2T = \Lambda$ and in a region of measure zero with a complex shape (Supplementary Information section IV B 5)^{21–25,31}. However, the fraction of multifractal states becomes vanishingly small only for extremely large system sizes of 10^7 sites^{25,31}. For system sizes relevant to our experiment and even to many conceivable condensed-matter experiments, our theoretical results clearly predict a non-zero fraction of multifractal states in an extended parameter range away from the duality line. This is consistent with earlier studies that had suggested that an extended multifractal regime persists in the thermodynamic limit²⁴. The existence and form of this anomalous regime are crucial for understanding our experimental measurements of the kAAH phase diagram. In particular, theory predicts that anomalous transport and re-entrant localization/delocalization transitions should emerge when $T, \Lambda/2 \geq 1$.

Figure 2 encompasses the first main result of our work: the experimental realization of the kAAH model. Figure 2a,b show the measured

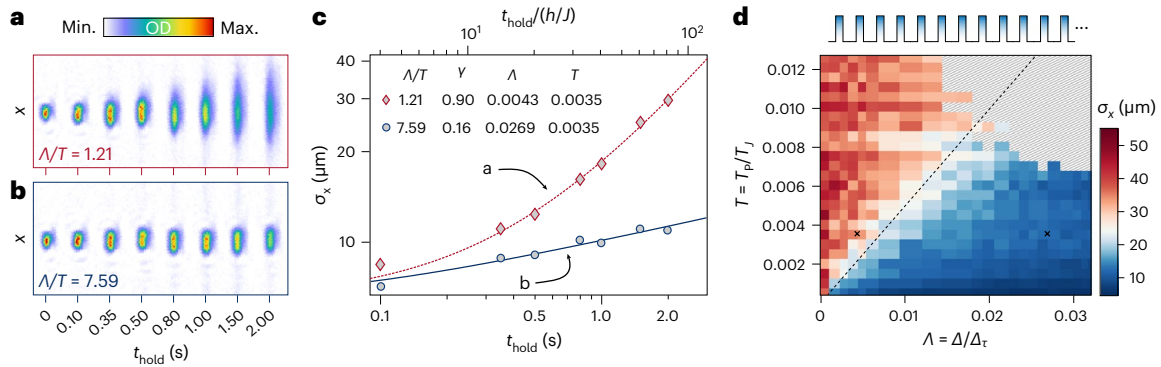


Fig. 2 | Realizing the kAAH model in the high-frequency regime. **a, b**, Time sequence of density profiles in the kicked lattice for Λ/T below **(a)** or above **(b)** the localization transition. **c**, Fitting expansion curves to a form that captures both short- and long-time behaviour at various (Λ, T) allows for measurement of the exponent γ . The curves are for the data in **a** and **b**. The extracted widths were fit to $\sigma_x(t) = \sigma_0(1 + t/t_0)^\gamma$, the solution to a generalized diffusion equation (Supplementary Information section III B). **d**, Measured localization phase diagram of the kAAH model for small Λ and T , using a simple rectangular form for the pulse shape $f_\tau(t)$ with $\tau = 1 \mu\text{s}$. The colour map depicts the fitted width of the density distribution σ_x as a function of Λ and T at $t_{\text{hold}} = 2 \text{ s}$. The dashed line

indicates the time-averaged static Aubry–André transition at $\Lambda/T = 2$. The centre point (white) of the colour map is set to the σ_x observed at the same hold time when the expansion exponent is in the centre of its transition from localized to delocalized values. Black crosses indicate the (Λ, T) values of the data in **a, b** and **c**. Cross-hatched pixels indicate data that failed cuts of the fitting procedure (Supplementary Information section III A) due to heating by interband transitions. Without mitigative measures, such heating prevents exploration of the phase diagram much beyond the region shown here. See Fig. 3 for details of the characterization and suppression of this effect. Max., maximum; Min., minimum; OD, optical density.

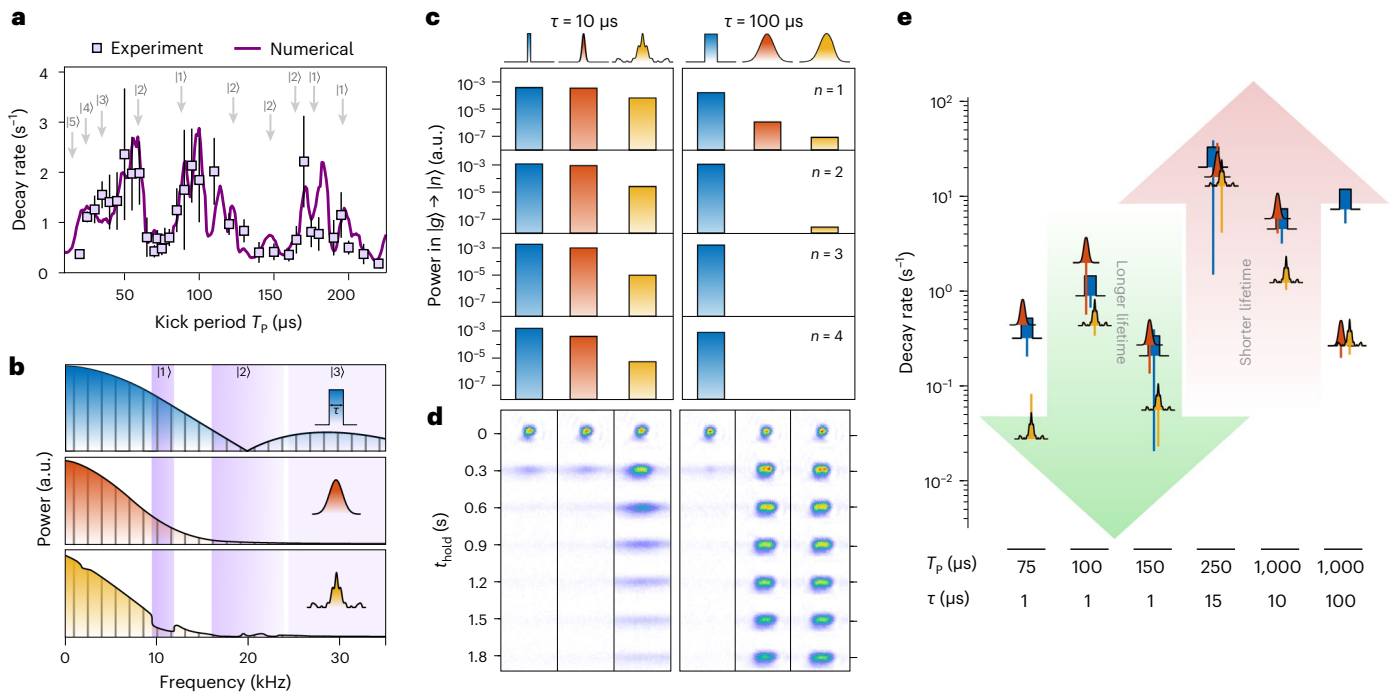


Fig. 3 | Apodized Floquet engineering. **a**, Decay rate of atoms kicked by square pulses with a pulse duration of $\tau = 1 \mu\text{s}$ and a kick strength of $\Lambda = 0.018$ for $t_{\text{hold}} = 2 \text{ s}$ as a function of kick period T_p . The solid curve is the result of a numerical calculation (Supplementary Information section IV A). Arrows indicate the dominant transitions from the ground band $|n = 0\rangle$ to excited bands $|n = 1, 2, \dots\rangle$ (see also Extended Data Fig. 2). Error bars represent 95% confidence intervals from an exponential fit to 20 measurements. **b**, Form of the power spectrum of square (top), Gaussian (middle) and filtered (bottom) pulses. Shaded areas represent interband transitions. The frequency comb spacing is not drawn to

scale for visibility. **c**, Net power in frequency ranges corresponding to interband transitions for square, Gaussian and filtered pulses of two pulse widths, each with period $T_p = 1 \text{ ms}$. For longer pulses, the Gaussian pulse already has little power in the interband transition frequencies and so filtering has little additional effect. **d**, Measured density profile at various times for each pulse shape. **e**, Measured decay rates from the ground band for different pulse shapes at various values of T_p and τ . The baseline of each symbol corresponds to the measured decay rate. Error bars represent 95% confidence bounds from an exponential fit. a.u., arbitrary units.

density evolution at two points in the phase diagram, one localized and one delocalized. The late-time width clearly distinguishes the two phases. The exponent γ characterizing the time evolution of the width σ_x of the density distribution ($\sigma_x \propto t^\gamma$ for large t) provides another diagnostic, with γ near 1 indicating delocalization and γ near zero indicating

localization (Fig. 2c). Deviations of measured values from exactly one or zero may be attributed to the finite duration of the experiment or to interparticle interactions, as discussed in Supplementary Information section II B. Figure 2d demonstrates the first experimental exploration of a swath of the kAAH phase diagram, obtained by

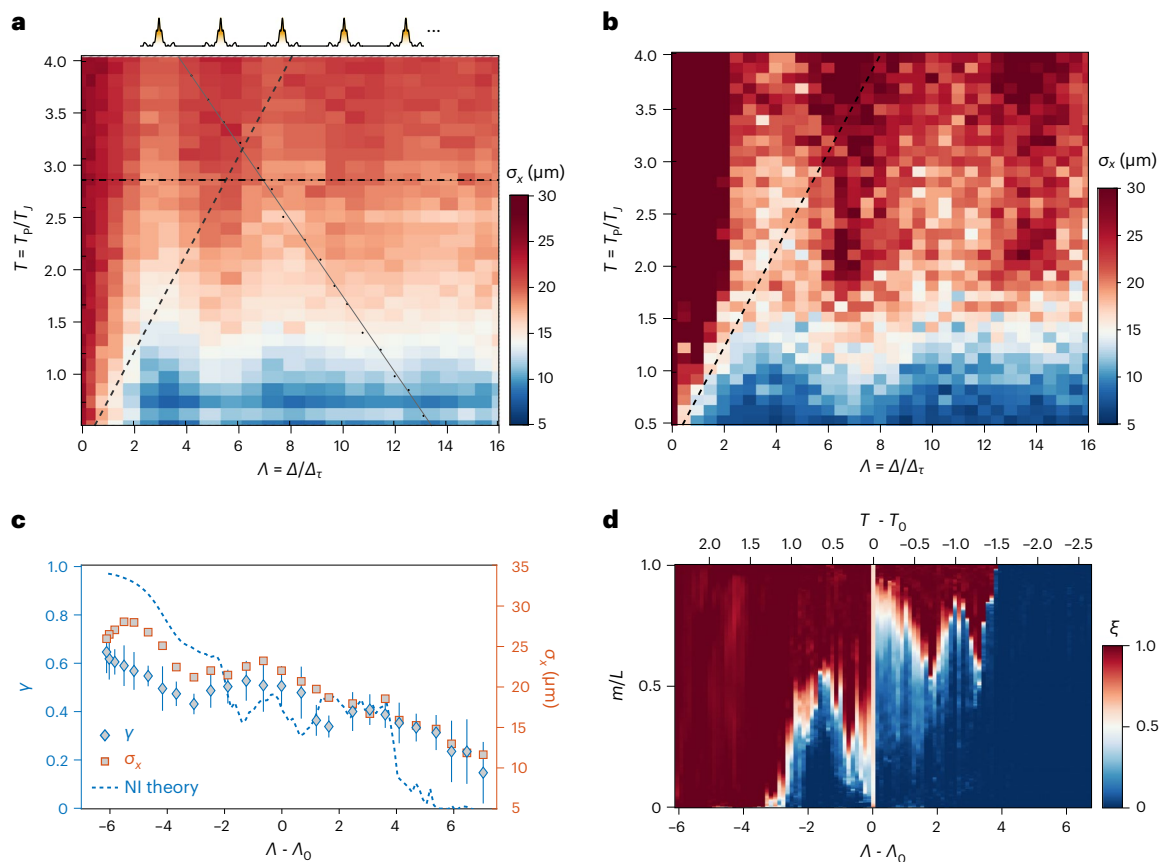


Fig. 4 | Experimental signatures of anomalous localization in the kAAH model. **a**, Measured phase diagram of the kAAH model for large T and Λ using apodized kicking waveforms (equivalent to a Gaussian with $\tau = 319.3 \mu\text{s}$). The colour map shows the fitted width of the density distribution σ_x for $t_{\text{hold}} = 2 \text{ s}$. The dashed line indicates the time-averaged static AAH transition at $\Lambda/T = 2$. The colour map centre (white) is chosen at this transition point as in Fig. 2d. **b**, Calculated phase diagram of the kAAH model for parameters and observable chosen to match the experiment. Numerically calculated time-evolved density distributions were convolved with the estimated point spread function of our imaging system and fitted with a Gaussian. The colour bar shows the fitted width

and has the same limits as **a**. **c**, Expansion exponent γ versus $\Lambda - \Lambda_0$ (diamonds) for parameter values indicated by points in **a**, extracted by fitting the late-time width evolution to $\sigma_x(t) \propto t^\gamma$. Error bars show 95% confidence bounds from such a fit to 16 measurements. The measured σ_x is also plotted (squares), indicating that this single measurement tracks well with fits of the full time series. Equivalent expansion exponent data for the horizontal dot-dashed line in **a** appears in Extended Data Fig. 5. NI, noninteracting. **d**, Scaling exponent ξ of the IPR for single-particle states as a function of disorder strength Λ for the same parameter range. m/L denotes the normalized index of eigenstates.

measuring the late-time width of the atomic density distribution for a range of values of T and Λ both $\ll 1$, using a simple rectangular form for the kick pulse shape $f_\tau(t)$. In accordance with expectations for this high-frequency regime, we observe a period-dependent localization transition near the Aubry–André critical point at $\Lambda/T = 2$. However, our quantum simulator using a rectangular $f_\tau(t)$ breaks down at values of T and Λ a hundred times smaller than those where the anomalous transport regime is predicted to emerge, due to higher-band excitations that invalidate the single-band approximation implicit in the kAAH model. This breakdown is visible in the cross-hatched data points near the upper right of Fig. 2d, which are (Λ, T) pairs where the density distribution failed experimental cuts (Supplementary Information section III A) on signal-to-noise ratio and centre position, indicating severe heating. Such interband heating prevents experimental access to the rich anomalous transport regime of the kAAH phase diagram; however, as we show next, this challenge can be overcome.

To extend the kAAH quantum simulator to the regime of the phase diagram with $T, \Lambda/2 \geq 1$ where anomalous behaviour is predicted, we developed a spectrally tailored (‘apodized’) Floquet engineering technique, which is the second main result of this work and which may prove useful in other contexts. Apodization is a filtering technique common in areas from optics to radio-frequency engineering. Here, we perform

an analogous procedure by changing the shape of the pulse function $f_\tau(t)$, thereby modifying the spectrum of the kicking waveform. The goal is to eliminate the population transfer to excited bands, which breaks the single-band assumption of the kAAH model. Figure 3a demonstrates the origin of this problem. Values of T_p higher than a few tens of microseconds give rise to the rapid decay of ground-band atoms. Peaks in the decay rate match numerically calculated rates of interband transfer, suggesting that the root cause of the heating is the overlap of the spectrum of the kicking waveform with interband transition frequencies (see also Extended Data Figs. 2 and 3). We investigated two approaches for eliminating the interband heating: (1) conventional apodization with a Gaussian window function and (2) spectral filtering of the pulse train to specifically remove interband transition frequencies. In both cases, the time-domain pulse shape $f_\tau(t)$ is renormalized to give equivalent pulse areas. Figure 3b,c shows the power spectra of different pulse shapes (square, Gaussian and spectrally filtered), superimposed (b) and integrated (c) over the frequency ranges of interband transitions, indicating that pulse shaping can address the problem of interband heating. Figure 3d shows experimental results for the density evolution with the three different pulse shapes for different pulse lengths τ , demonstrating the substantially better performance of shaped pulses, and Fig. 3e shows the measured decay rate for different

pulse shapes, kick periods and repetition rates. Longer lifetimes are consistently achieved by spectrally engineering the kicking pulse shape. For the kAAH model, apodized Floquet engineering is absolutely required for accessing the non-trivial regions of the phase diagram at large T and Λ with quantum gas experiments.

Figure 4a shows phase map data from such an apodized quantum simulator including the predicted anomalous transport regime. Although the time-averaged Aubry–André phase transition at $\Lambda/T = 2$ is visible for small T , areas of anomalous localization and delocalization appear at larger T , in qualitative agreement with theoretical predictions. As the disorder strength is increased for $T > 1.5$, the system appears to localize. Then it exhibits re-entrant disorder-driven delocalization and finally localizes again at strong disorder. Both these features agree with phase maps of an equivalent measurement on a numerically simulated kAAH model, shown in Fig. 4b. A simpler but less experimentally motivated map of the same numerical results appears in Extended Data Fig. 4, which maps the second moment of the density distribution without any convolution or fit. Although the fine details of the phase map depend on the specific quantity plotted, features like the small- T Aubry–André transition, the anomalous regime and re-entrant delocalization are always observed. To further investigate this newly realized state of driven matter, we measured the full expansion dynamics at selected points on the phase diagram. The transport scaling exponent γ serves as a signature of localized, delocalized and multifractal states in the kAAH model (Supplementary Information section IV B 6)^{22,29,30}. Transport can also be diagnosed in the numerics by the time evolution of the IPR of the real-space density profile (Supplementary Information section IV B 2). As shown in Fig. 4c, across a broad swath of the phase diagram, the transport exponent lies between 0.4 and 0.6, which, based on the results of our theoretical calculations, we attribute to the presence of multifractal states. Our experimental observations accord with theoretical predictions also plotted in Fig. 4c. Here we note two important subtleties. First, states in the regime between the completely localized and completely delocalized areas have mixed character (Fig. 4d), and for any non-zero fraction of delocalized states, transport at the longest timescales is expected to be ballistic. However, for experimentally relevant system sizes, the theoretically predicted presence of multifractal states leads to sub-ballistic transport persisting up to timescales much longer than those explored experimentally (Supplementary Information section IV B 5). Second, note that continuously varying transport exponents can also arise in disordered systems due to rare regions in which the system locally resembles a localized state³³. However, in a quasiperiodic system such as ours, such rare regions do not exist³⁴.

These results represent the first experimental glimpse, to our knowledge, of the rich phase diagram of a prototypical model of localization in driven quantum matter. The simple but unexpectedly powerful apodization techniques we demonstrate could be applied in a broad range of contexts and may enhance the range of quantum simulators in any situation in which a kicked system emulates a single-band model³⁵. The results raise several fascinating questions for future investigation. How can multifractality and extended criticality be directly experimentally probed? Is the observed anomalous regime stable against the introduction of interactions^{19,28,36} or the presence of gapless propagating modes such as phonons? Can the duality of the phase map be directly imaged? In the low-frequency regime, the Floquet Hamiltonian is generically long-ranged, and the appearance of an anomalous transport phase recalls predictions of such phases in Hamiltonians with long-range hopping³⁷. This raises the possibility of engineering other long-range Hamiltonians using the techniques of apodized low-frequency Floquet engineering presented here, potentially allowing the study of phenomena unattainable with local Hamiltonians such as robust error-correcting quantum codes³⁸. A final intriguing possibility for future work is the realization of related anomalous states in Floquet-engineered solids or solid-state heterostructures³⁹.

Online content

Any methods, additional references, Nature Portfolio reporting summaries, source data, extended data, supplementary information, acknowledgements, peer review information; details of author contributions and competing interests; and statements of data and code availability are available at <https://doi.org/10.1038/s41567-023-02329-4>.

References

1. D'Alessio, L., Kafri, Y., Polkovnikov, A. & Rigol, M. From quantum chaos and eigenstate thermalization to statistical mechanics and thermodynamics. *Adv. Phys.* **65**, 239–362 (2016).
2. Abanin, D. A., Altman, E., Bloch, I. & Serbyn, M. Colloquium: many-body localization, thermalization, and entanglement. *Rev. Mod. Phys.* **91**, 021001 (2019).
3. Gogolin, C. & Eisert, J. Equilibration, thermalisation, and the emergence of statistical mechanics in closed quantum systems. *Rep. Prog. Phys.* **79**, 056001 (2016).
4. Mori, T., Ikeda, T. N., Kaminishi, E. & Ueda, M. Thermalization and prethermalization in isolated quantum systems: a theoretical overview. *J. Phys. B* **51**, 112001 (2018).
5. Evers, F. & Mirlin, A. D. Anderson transitions. *Rev. Mod. Phys.* **80**, 1355 (2008).
6. Richardella, A. et al. Visualizing critical correlations near the metal–insulator transition in $\text{Ga}_{1-x}\text{Mn}_x\text{As}$. *Science* **327**, 665–669 (2010).
7. Chabé, J. et al. Experimental observation of the Anderson metal–insulator transition with atomic matter waves. *Phys. Rev. Lett.* **101**, 255702 (2008).
8. Amin, K. R., Nagarajan, R., Pandit, R. & Bid, A. Multifractal conductance fluctuations in high-mobility graphene in the integer quantum Hall regime. *Phys. Rev. Lett.* **129**, 186802 (2022).
9. Weitenberg, C. & Simonet, J. Tailoring quantum gases by Floquet engineering. *Nat. Phys.* **17**, 1342–1348 (2021).
10. Aubry, S. & André, G. Analyticity breaking and Anderson localization in incommensurate lattices. *Ann. Isr. Phys. Soc.* **3**, 18 (1980).
11. Harper, P. G. Single band motion of conduction electrons in a uniform magnetic field. *Proc. Phys. Soc. Sec. A* **68**, 874 (1955).
12. Hofstadter, D. R. Energy levels and wave functions of Bloch electrons in rational and irrational magnetic fields. *Phys. Rev. B* **14**, 2239–2249 (1976).
13. Azbel, M. Y. Quantum particle in one-dimensional potentials with incommensurate periods. *Phys. Rev. Lett.* **43**, 1954 (1979).
14. Roati, G. et al. Anderson localization of a non-interacting Bose–Einstein condensate. *Nature* **453**, 895–898 (2008).
15. Lucioni, E. et al. Observation of subdiffusion in a disordered interacting system. *Phys. Rev. Lett.* **106**, 230403 (2011).
16. Kraus, Y. E., Lahini, Y., Ringel, Z., Verbin, M. & Zilberberg, O. Topological states and adiabatic pumping in quasicrystals. *Phys. Rev. Lett.* **109**, 106402 (2012).
17. Bordia, P., Lüschen, H., Schneider, U., Knap, M. & Bloch, I. Periodically driving a many-body localized quantum system. *Nat. Phys.* **13**, 460–464 (2017).
18. Lüschen, H. P. et al. Single-particle mobility edge in a one-dimensional quasiperiodic optical lattice. *Phys. Rev. Lett.* **120**, 160404 (2018).
19. An, F. A. et al. Interactions and mobility edges: observing the generalized Aubry–André model. *Phys. Rev. Lett.* **126**, 040603 (2021).
20. Gadway, B., Reeves, J., Krinner, L. & Schneble, D. Evidence for a quantum-to-classical transition in a pair of coupled quantum rotors. *Phys. Rev. Lett.* **110**, 190401 (2013).
21. Artuso, R., Borgonovi, F., Guarneri, I., Rebuzzini, L. & Casati, G. Phase diagram in the kicked Harper model. *Phys. Rev. Lett.* **69**, 3302 (1992).

22. Artuso, R., Casati, G. & Shepelyansky, D. Fractal spectrum and anomalous diffusion in the kicked Harper model. *Phys. Rev. Lett.* **68**, 3826 (1992).
23. Leboeuf, P., Kurchan, J., Feingold, M. & Arovas, D. P. Phase-space localization: topological aspects of quantum chaos. *Phys. Rev. Lett.* **65**, 3076–3079 (1990).
24. Borgonovi, F. & Shepelyansky, D. Spectral variety in the kicked Harper model. *Europhys. Lett.* **29**, 117–122 (1995).
25. Prosen, T., Satija, I. I. & Shah, N. Dimer decimation and intricately nested localized-ballistic phases of a kicked Harper model. *Phys. Rev. Lett.* **87**, 066601 (2001).
26. Qin, P., Yin, C. & Chen, S. Dynamical Anderson transition in one-dimensional periodically kicked incommensurate lattices. *Phys. Rev. B* **90**, 054303 (2014).
27. Čadež, T., Mondaini, R. & Sacramento, P. D. Dynamical localization and the effects of aperiodicity in Floquet systems. *Phys. Rev. B* **96**, 144301 (2017).
28. Zhang, Y., Zhou, B., Hu, H. & Chen, S. Localization, multifractality, and many-body localization in periodically kicked quasiperiodic lattices. *Phys. Rev. B* **106**, 054312 (2022).
29. Ketzmerick, R., Kruse, K., Kraut, S. & Geisel, T. What determines the spreading of a wave packet? *Phys. Rev. Lett.* **79**, 1959 (1997).
30. Roy, S., Khaymovich, I. M., Das, A. & Moessner, R. Multifractality without fine-tuning in a Floquet quasiperiodic chain. *SciPost Phys.* **4**, 25 (2018).
31. Ketzmerick, R., Kruse, K. & Geisel, T. Efficient diagonalization of kicked quantum systems. *Phys. D* **131**, 247–253 (1999).
32. Roy, S., Mishra, T., Tanatar, B. & Basu, S. Reentrant localization transition in a quasiperiodic chain. *Phys. Rev. Lett.* **126**, 106803 (2021).
33. Agarwal, K., Gopalakrishnan, S., Knap, M., Müller, M. & Demler, E. Anomalous diffusion and Griffiths effects near the many-body localization transition. *Phys. Rev. Lett.* **114**, 160401 (2015).
34. Gopalakrishnan, S. & Parameswaran, S. Dynamics and transport at the threshold of many-body localization. *Phys. Rep.* **862**, 1–62 (2020).
35. Liu, T., Xia, X., Longhi, S. & Sanchez-Palencia, L. Anomalous mobility edges in one-dimensional quasiperiodic models. *SciPost Phys.* **12**, 27 (2022).
36. Sarkar, M., Ghosh, R., Sen, A. & Sengupta, K. Signatures of multifractality in a periodically driven interacting Aubry–André model. *Phys. Rev. B* **105**, 024301 (2022).
37. Deng, X., Ray, S., Sinha, S., Shlyapnikov, G. & Santos, L. One-dimensional quasicrystals with power-law hopping. *Phys. Rev. Lett.* **123**, 025301 (2019).
38. Hamma, A., Castelnovo, C. & Chamon, C. Toric-boson model: toward a topological quantum memory at finite temperature. *Phys. Rev. B* **79**, 245122 (2009).
39. Basov, D., Averitt, R. & Hsieh, D. Towards properties on demand in quantum materials. *Nat. Mater.* **16**, 1077–1088 (2017).

Publisher's note Springer Nature remains neutral with regard to jurisdictional claims in published maps and institutional affiliations.

Open Access This article is licensed under a Creative Commons Attribution 4.0 International License, which permits use, sharing, adaptation, distribution and reproduction in any medium or format, as long as you give appropriate credit to the original author(s) and the source, provide a link to the Creative Commons license, and indicate if changes were made. The images or other third party material in this article are included in the article's Creative Commons license, unless indicated otherwise in a credit line to the material. If material is not included in the article's Creative Commons license and your intended use is not permitted by statutory regulation or exceeds the permitted use, you will need to obtain permission directly from the copyright holder. To view a copy of this license, visit <http://creativecommons.org/licenses/by/4.0/>.

© The Author(s) 2024

Methods

Preparing the initial state

The experiments began by preparing a BEC of ^{84}Sr by evaporation in a crossed dipole trap with trapping frequencies of 50 and 70 Hz in the horizontal and vertical directions, respectively. The BEC was adiabatically loaded over 250 ms into a primary optical lattice with an initial width of 6 μm . The lattice was formed by retro-reflecting a small portion of a 1,064 nm beam, thereby creating a lattice potential superimposed on a single-beam dipole trap. This non-reflected portion of the beam produced most of the transverse confinement with a transverse trapping frequency near 100 Hz and a weak longitudinal confinement with a trapping frequency near 0.3 Hz. The dynamics were initiated by suddenly removing the axial confinement due to the crossed dipole trap.

Implementing the kAAH Hamiltonian

The incommensurate kicking lattice formed by $\lambda_s = 915$ nm light was superimposed onto the primary lattice as a periodic pulse train. The pulse intensity, pulse width and pulse waveform were controlled by tailoring the radio-frequency waveform sent to the acousto-optic modulator used to modulate the 915 nm light intensity. Lattice depths were calibrated by Kapitza–Dirac diffraction. The depth of the primary lattice was stabilized to $10E_r$, unless otherwise specified. The time-dependent depth of the kicking lattice was monitored by a photodiode and recorded. The 1,064 and 915 nm standing waves shared a retro-reflecting mirror, which passively stabilized the relative phase of the two lattices.

Generating apodized waveforms

To obtain driving waveforms that do not drive excitation to higher bands, unwanted frequency components were filtered out of initial trial waveforms (either Gaussian or square pulses) by repeated application of appropriate digital band-pass filters, setting negative amplitudes to zero for physical realizability. The resulting waveform was used as an envelope for the radio-frequency signal sent to the acousto-optic modulator that controlled the power of the kicking lattice beam. For large T values ($T_p > 1$ ms), simply using a Gaussian waveform was equally effective, as shown in Fig. 3.

Data processing

The density distribution after a time evolution of up to 2 s in the kicked lattice was obtained by analysing in situ absorption images. The width of the distribution was extracted from a Gaussian fit to the transversely integrated density profile. Data were omitted (hashed points in Fig. 2a) if the centre position of this fit differed substantially from the mean and if the signal-to-noise ratio was less than 40% of the mean. These cuts were failed for experimental realizations that produced density profiles so sparse as to not be reliably fitted and analysed. This was generally due to atom loss associated with substantial transverse or higher-band excitation. As discussed in the manuscript and Supplementary Information, we were able to identify the specific excitations that were being resonantly driven for all areas where the cuts were failed. See Supplementary Information section III for quantitative details of this procedure.

Data availability

The data that support the findings of this study are available from the corresponding author upon reasonable request.

Code availability

The codes used for data analysis and numerical simulation are available from the corresponding author upon reasonable request.

Acknowledgements

We thank L. Sanchez-Palencia, D. Arovos and A. Eckardt for helpful conversations. This material is based upon optical lattice emulator work principally led and supported by the US Department of Energy, Office of Science, National Quantum Information Science Research Centers, Quantum Science Center. Quantum control aspects of the work were supported by the Air Force Office of Scientific Research (FA9550-20-1-0240), the Army Research Office (MURI W911NF1710323), the Eddleman Center for Quantum Innovation and the Quantum Leap Challenge Institutes of the National Science Foundation (NSF; Grant No. OMA-2016245 to D.M.W.). A.R.D. acknowledges support from the NSF Quantum Foundry at the University of California, Santa Barbara, funded by the Q-AMASE-i programme (Grant No. DMR1906325). T.G. is supported by an Alfred P. Sloan Research Fellowship and the NSF (Grant No. DMR-1752417). T.-C.L. acknowledges support from the Perimeter Institute for Theoretical Physics. Research at the Perimeter Institute is supported in part by the Government of Canada through the Department of Innovation, Science and Economic Development and by the Province of Ontario through the Ministry of Colleges and Universities.

Author contributions

T.S., M.P., H.E.K., J.E.P., Y.B., P.D., A.C. and A.R.D. ran the experiment and performed the measurements. T.S., M.P., H.E.K., J.E.P., Y.B. and P.D. analysed the data. H.E.K., Y.B. and T.-C.L. performed the theoretical calculations. T.S., M.P., H.E.K., J.E.P., Y.B., P.D., A.C. and D.M.W. developed the idea for the experiment. D.M.W. supervised the work. T.S., M.P., H.E.K., J.E.P., Y.B., P.D., A.C., T.-C.L., T.G. and D.M.W. wrote the manuscript. All authors contributed to the discussion and interpretation of the results.

Competing interests

The authors declare no competing interests.

Additional information

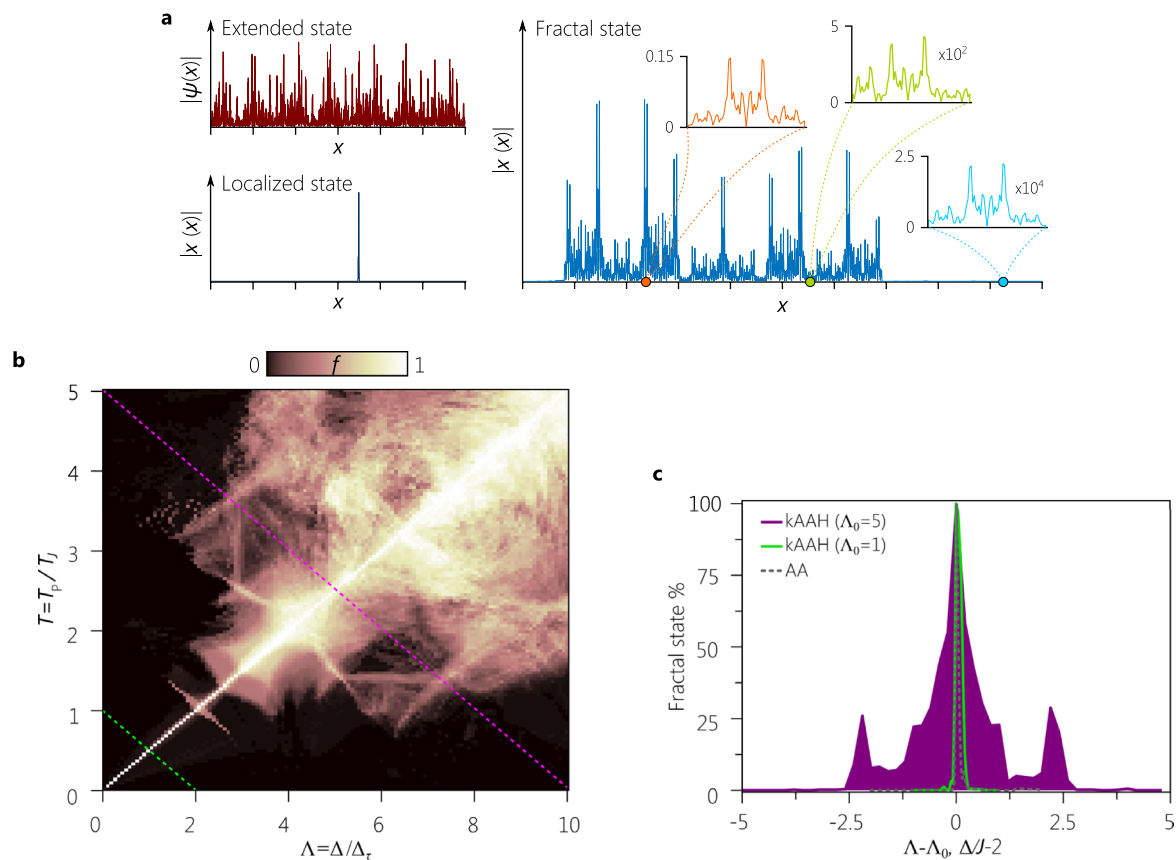
Extended data Extended data are available for this paper at <https://doi.org/10.1038/s41567-023-02329-4>.

Supplementary information The online version contains supplementary material available at <https://doi.org/10.1038/s41567-023-02329-4>.

Correspondence and requests for materials should be addressed to David M. Weld.

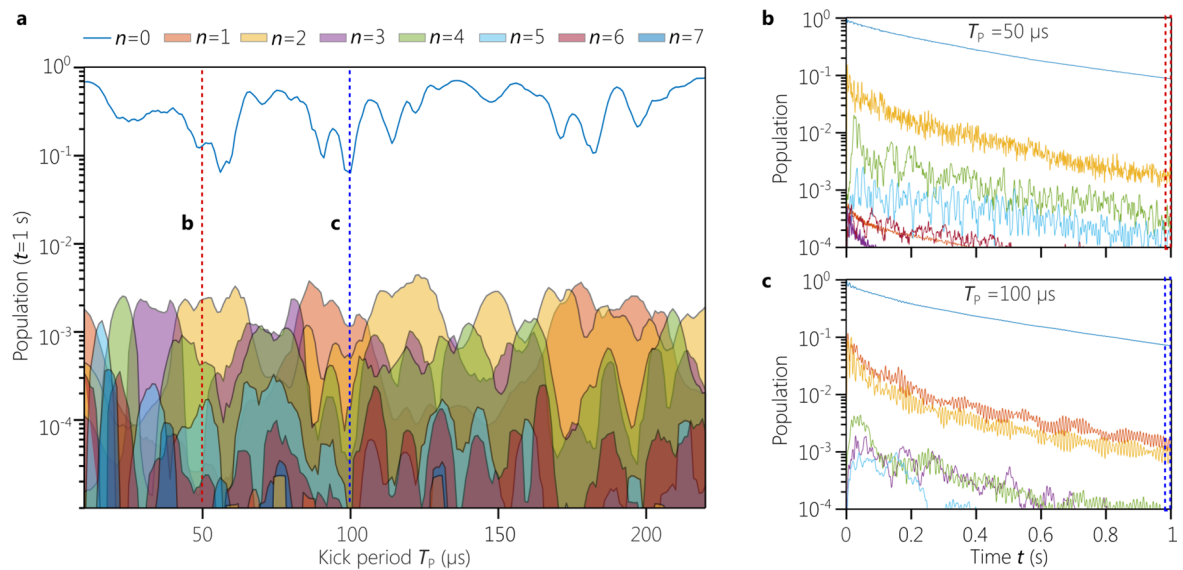
Peer review information *Nature Physics* thanks the anonymous reviewers for their contribution to the peer review of this work.

Reprints and permissions information is available at www.nature.com/reprints.



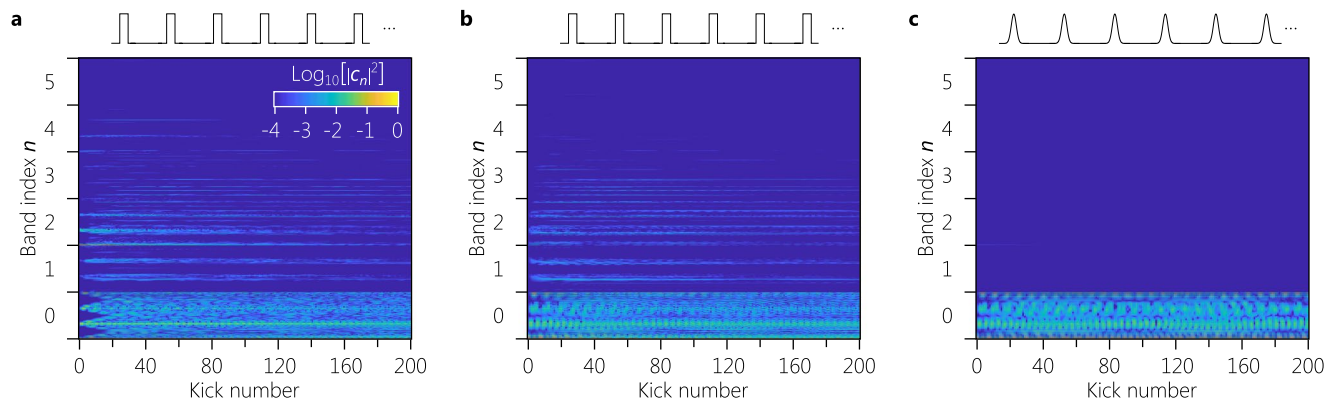
Extended Data Fig. 1 | Multifractality in the kicked Aubry-André-Harper model. **a**, Examples of extended, localized, and fractal (self-similar) wavefunctions. **b**, Calculated phase diagram of the kAAH model for $\alpha = 1.162842$. Colorbar shows the percentage of multifractal states, defined operationally by the inequality $0.1 < \xi < 0.9$, versus normalized kick period $T = T_p/T_j$ and kick strength Λ . ξ is the IPR scaling exponent. **c**, Percentage of multifractal states

versus Λ , for the static AAH model and the two line cuts of the kAAH phase diagram indicated by dotted lines in **b**. Λ_0 corresponds to the point where $\Lambda = T/2$. In the static and rapidly kicked models, fractality occurs only at the phase transition $\Delta J = 2$ and $\Lambda = T/2$, respectively, while at high kick periods an extended multifractal regime emerges.



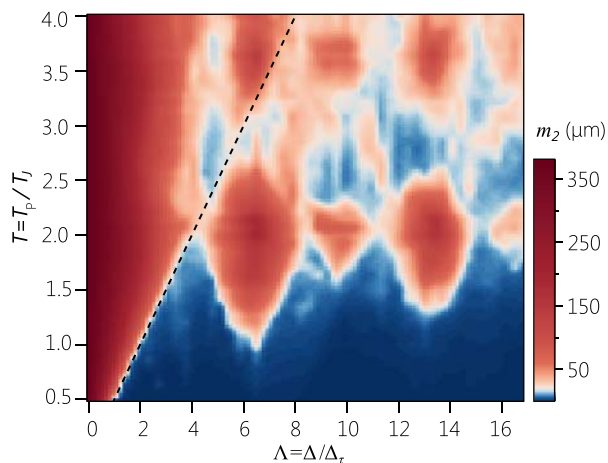
Extended Data Fig. 2 | Multiband time-domain simulations. Results of numerically simulating band population for 1 s of kicking with 1μ s square pulses. **a**, Band population distribution as a function of kick period T_p for the ground

and excited bands at $t=1$ s. **b-c**, Examples of population dynamics for $T_p = 50 \mu$ s (**b**) and $T_p = 100 \mu$ s (**c**). See Supplementary Information Sec. IV A for details of numerical simulations.

**Extended Data Fig. 3 | Spread of the excited eigenmodes with kicking.**

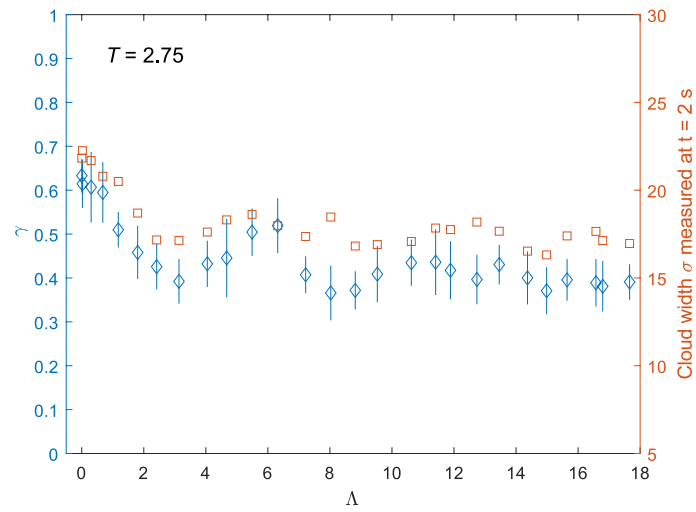
a, b, Numerical simulations of eigenmode occupation evolution during square-pulse kicking with $\tau = 100 \mu\text{s}$ and $T_p = 1 \text{ ms}$ for **(a)** diabatic and **(b)** adiabatic loading of the primary optical lattice. y-axis tick marks correspond to band boundaries. **c,** Eigenmode occupation evolution during Gaussian-pulse kicking

with equivalent pulse area and kicking period to those of **a** and **b**. The primary lattice is adiabatically loaded. While in **a** and **b**, the kicking results in excitation to higher bands, in **c**, excitations are mainly confined to the ground band. See Supplementary Information Sec. IV A for details of numerical simulations.



Extended Data Fig. 4 | Numerically calculated phase diagram of the kAAH model. Numerically calculated second moment of the density distribution of particles evolving under the kAAH model is shown for parameters and initial conditions chosen to match those of the experiment. The underlying simulations are identical to those for which an experimentally-motivated Gaussian fit is plotted in Fig. 4. Qualitatively the two maps exhibit the same localized, delocalized, and intermediate regimes, but some quantitative differences are

apparent. The difference in the maps stems from the non-normal character of the density distributions in delocalized and intermediate areas, where the second moment can be dominated by small populations at large distances. The map is averaged over 40 randomly chosen phases φ of the quasiperiodic potential, though this does not substantially affect the result (see Supplementary Information Sec. IV B 1).



Extended Data Fig. 5 | Transport measurement of the expansion. Measured expansion exponent γ and fixed-time width are shown for (T, Λ) points on the horizontal dot dashed line in Fig. 4(a). γ is extracted by fitting the late-time width

evolution to $\sigma_x(t) \sim t^\gamma$ in the same procedure as Fig. 4(c). Error bars for each data point are 95% confidence bounds from the curve fit to a time-series data set consisting of 11 data points.